Construction of a dilution refrigerator cooled scanning force microscope

A. E. Gildemeister,[a] T. Ihn, C. Barengo, P. Studerus, and K. Ensslin
Laboratory of Solid State Physics, ETH Zürich, CH-8093 Zürich, Switzerland

We present a scanning force microscope that operates in a dilution refrigerator at temperatures of about 100 mK. We use tuning fork sensors for scanning gate experiments on mesoscopic semiconductor nanostructures. Slip-stick motors allow sample coarse-positioning at base temperature. The construction, thermal anchoring, and a procedure to optimize the settings of the phase-locked loop that we use for sensor control are discussed in detail. We present low-temperature topographic and scanning gate images as examples of successful operation. © *2007 American Institute of Physics.* [DOI: 10.1063/1.2431793]

I. INTRODUCTION

It is desirable to cool scanning force microscopes (SFMs) to very low temperatures either to improve the force sensitivity (e.g., Ref. 1) or to study samples that only function at low temperatures. While liquid helium SFMs are now commercially available and several scanning tunneling microscopes for dilution refrigerators have been reported (Ref. 2 and references therein), to date only a handful of SFMs was built for dilution refrigerators.[3–7]

We have constructed a SFM that operates at temperatures around 100 mK, allows sample coarse positioning at base temperature, and uses a piezoelectric tuning fork with a thin wire glued to one prong as a nonoptical sensor[8,9] which allows the study of light-sensitive samples.

Our instrument is dedicated to the study of electronic transport in mesoscopic semiconductor nanostructures. Here, microscopy helps one to understand transport locally, whereas standard transport measurements provide spatially averaged information. Typically, we use the metallic tip of the microscope as a scanned gate, interacting with structures underneath. This technique has been successfully used to image the branched flow of electrons through a small constriction,[10] to image and manipulate single electrons in carbon nanotubes[11] as well as in nanostructures based on two-dimensional electron gases (2DEGs),[12,13] and, recently, to study the Aharonov-Bohm effect.[14]

At lower temperatures more effects can be studied microscopically. For example, access to the individual energy eigenstates of quantum dots could allow one to measure the local density of states.[15]

II. THE SETUP

The microscope fits into a KelvinoxMX 100 dilution refrigerator from Oxford Instruments operated in a ^{4}He Dewar with an 8 T superconducting magnet. The Dewar rests on a foundation that is detached from the building to reduce vibrations. The microscope and the dilution unit are mechanically coupled to the Dewar and mounted in the inner vacuum chamber (IVC) which contains about 1 cm^3 He exchange gas. At temperatures below 8 K the exchange gas is cryopumped to produce the high vacuum necessary for running the dilution unit. We heat the sample while cooling down to avoid that any residual gas in the IVC condenses on the sample. In contrast to some other instruments (e.g., Ref. 16), our setup does not feature a system for *in situ* sample preparation.

A. Microscope

Figure 1 shows the microscope, consisting of two main components, the *x-y* table at the top and the *z* module at the bottom. The sample is mounted in a ceramic chip carrier which fits into the chip socket at the bottom of the *x-y* table. The *z* module comprises the sensor, the scan piezo, and the Macor tube holding the piezo. The upside-down geometry reduces the contamination of the sample surface by dust particles. The different components are mounted in a rigid single-piece CuBe frame.

The *x-y* table contains a Pt100-, an Allen-Bradley-, and a RuO$_2$ thermometer to cover the instrument's temperature range. A resistive wire allows *in situ* heating of the sample to room temperature, and a LED can illuminate the sample. The chip socket connects to 24 coaxial cables. Five of these allow driven-shield operation which increases the bandwidth by a factor of about 5 compared to operation with a grounded shield.

Slip-stick motors allow lateral coarse positioning with a range of about 3 mm at low temperatures. For this we use three 16 mm long piezo tubes [3.175 mm diameter (1/8 in.), EBL4 from Staveley Sensors] that are glued perpendicular to the plane of motion. Small sapphire spheres are glued to both ends of each tube. These support stainless-steel caps which are polished and coated with Balinit C/WC. The tubes with the caps are sandwiched between two sapphire surfaces that are clamped together by a spring. These form the *x-y* table and support the sample mount.

For coarse motion of the *z* module we use six piezo stacks that hold the Macor tube. The sliding surfaces are made of sapphire on the tube and ZrO$_2$ on the piezo stacks. A spring compensates the relatively high weight of the Macor.

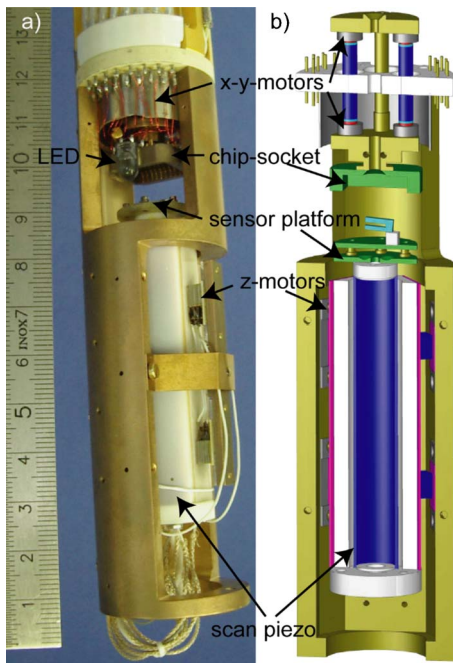[a] Electronic mail: gildemeister@phys.ethz.ch

FIG. 1. (Color online) (a) A photograph and (b) a sectional drawing of the microscope. It connects to the mixing chamber at the top.

For scanning we use a 63.5 mm (2.5 in.) long piezo tube of 9.53 mm (3/8 in.) diameter (EBL3 from Staveley Sensors). At base temperature the scan range is about 7 $\times 7$ μm^2 and the z range is about ± 400 nm when applying ± 70 V. Depolarization effects occur when these voltages are roughly tripled.

We use a tuning fork sensor that can be seen in Fig. 2(a). We remove all magnetic parts from a commercial 32 kHz tuning fork and glue it onto a small ceramic support, such that both prongs can oscillate. Then, we glue a 15 μm PtIr wire to one of the prongs and electrochemically etch it to sharpen the tip. Figure 2(b) shows a scanning electron microscope image of a typical tip with an apex diameter of about 40 nm. At base temperature these sensors have typical quality factors of about 150 000.

Our samples are mounted on chip carriers that connect to up to 24 coaxial cables; a chip carrier may contain multiple samples. Exchanging the chip carrier or the sensor requires warming up the dilution unit and breaking the vacuum.
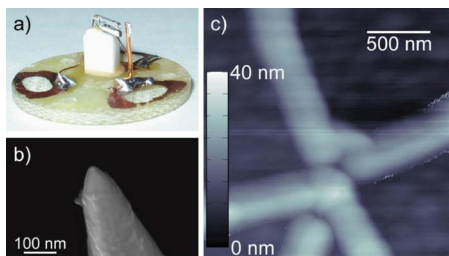

FIG. 2. (Color online) (a) The sensor: A tuning fork on a small support with a wire glued to one prong. The circuit board diameter is 18 mm. (b) An electron-beam micrograph of a PtIr scanning tip. (c) Topography scan, taken during cooldown 2, showing a quantum dot and an adjacent quantum point contact defined by local anodic oxidation on the surface of a GaAs/AlGaAs heterostructure.

TABLE I. The mixing chamber temperature T_{MC}, sample temperature T_S, electron temperature T_e, first cable temperature T_{C1}, and second cable temperature T_{C2} measured in four different cooldowns. All temperatures are in millikelvin (mK) and the accuracy is about ± 15 mK.

Cooldown	T_{MC}	T_S	T_e	T_{C1}	T_{C2}
1	260	570	510	-	-
2	65	300	-	-	-
3	40	100	-	80	80
4	40	200	220	-	-

B. Cabling, thermal anchoring, and thermometry

The refrigerator's cooling power is 100 μW at 100 mK and it drops quickly for lower temperatures. Electrical transport measurements and SFM operation require many cables connecting sample and microscope with control electronics at room temperature. Heat conduction of the cables and high-frequency (HF) noise contribute to sample heating. We reduce these effects by thermally anchoring the cables at points with higher cooling power and by carefully filtering against HF noise.

We use 24 twisted-pair constantan cables for thermometry and heating, 12 superconducting cables (CRYC from Lakeshore) for the high voltages applied to the piezos, and 30 semirigid stainless-steel coax cables (UT 20-SS-SS from Microcoax) for transport measurements. The constantan cables do not heat the mixing chamber significantly and, while the heating power due to the superconducting cables is below 10 μW, we estimate the heating power of the coax cables to be about 1 mW without thermal anchors. Anchoring the cables at the 1.7 K stage reduces the estimated heat load on the mixing chamber to 5 μW. Another anchor at the mixing chamber ensures the thermal link to the sample.

We anchor the constantan and CRYC cables by bringing them in close contact with larger metallic parts of the refrigerator and by tightly winding copper wire around them. Anchors for the coaxial cables are realized by connecting the center conductor to a thin insulated wire that is wound around a small metal cylinder and covered with silver paint. This solenoid coil also acts as a low-pass filter with a cutoff frequency of about 400 MHz.

The temperatures that have been reached with the instrument depended on details that varied between cooldown cycles, such as the number of cables connected to the sample or the way these cables touched various parts of the microscope. They leave room for improvement. Table I shows the different temperatures we have measured in four different cooldowns. Usually we measure temperatures with two RuO$_2$ thermometers: the built-in thermometer of the refrigerator that measures the temperature of the mixing chamber T_{MC} and the thermometer measuring the sample holder's temperature T_S. During cooldowns 1 and 4 the sample, a quantum dot, also allowed us to measure the electronic temperature T_e. During cooldown 3 no sample was mounted and instead two temporarily installed thermometers allowed us to measure the temperature of the coaxial cables. The first thermometer measured T_{C1} at the thermal anchors near the mixing chamber and the second thermometer measured the temperature T_{C2} just before the cables connect to the sample.
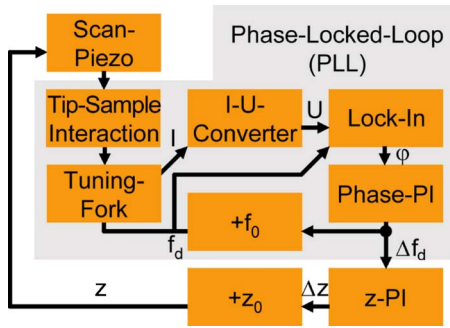
FIG. 3. (Color online) Schematic of the PLL (gray box) and the z feedback.

Scanning does not affect the temperature, whereas the coarse positioning motors may heat up the sample by several hundred millikelvin.

C. Electronics

For transport measurements and sensor control we use homebuilt preamplifiers operating at room temperature. They are installed in a HF-tight box mounted at the top of the Dewar, thereby preventing noise pickup on the long cables from the Dewar to the instrument rack. Using differential inputs eliminates ground loops.

The Nanonis system that we use for controlling the microscope[17] features a digital phase-locked loop, a real-time computer for all time-critical operations, and user-friendly software.

III. OPTIMIZING THE FEEDBACK

A. Phase-locked loop

Phase-locked loops (PLLs) are frequently employed to increase the bandwidth in the detection of forces with tuning fork sensors. We have measured the transfer function of the Nanonis PLL and modeled it using linear control theory. As a result we can now choose optimal feedback parameters before the tip touches the surface, hence avoiding tip crashes caused by poor feedback parameters. The Appendix provides a detailed derivation of the results presented in this section.

Figure 3 shows a schematic of the PLL and the additional feedback for the scan piezo. Initially, we drive the tuning fork at its resonance frequency. Now, a force between tip and surface changes the resonance frequency of the tuning fork. This creates a phase shift between the driving voltage and the current through the tuning fork. We convert the current into a voltage and detect the phase shift with respect to the driving voltage in a lock-in amplifier. Shaped by a proportional and integral controller (PIC), we use the phase shift to adjust the driving frequency to the new resonance frequency of the tuning fork. In a second feedback loop the distance between tip and surface is controlled to keep the frequency shift and hence the force constant.

The tuning fork sensor has a characteristic response bandwidth

$$f_c := -\left(\frac{\partial \varphi}{\partial f_d}\right)_{f_d = f_{\text{res}}}^{-1} = \frac{f_{\text{res}}}{2Q}, \tag{1}$$

where f_d is the driving frequency, f_{res} is the resonance frequency and Q is the quality factor of the tuning fork sensor. Since f_c can vary by more than an order of magnitude for different sensors and also as a function of temperature, it has to be measured every time the conditions change. A given sensor may have a bandwidth of several hertz at room temperature but only 0.1 Hz at base temperature.

The PIC has a characteristic frequency

$$f_{\text{PI}} = \frac{I}{2\pi P} = \frac{1}{2\pi T}, \tag{2}$$

where I and P are the integral and proportional constants and T is the time constant.[18] The frequency f_{PI} can be directly adjusted in the experiment. To maximize the PLL bandwidth while retaining a stable (i.e., nonoscillatory) feedback we set $f_{\text{PI}} = f_c$, i.e.,

$$T = \frac{1}{2\pi f_c}. \tag{3}$$

In this case the PLL transfer function $L(f)$ [cf. Eq. (A4)] reduces to a first-order low-pass filter with bandwidth P as shown in Figs. 4(a)–4(d). Figures 4(a) and 4(b) also show the undesirable effects of $f_{\text{PI}} \lessgtr f_c$, an overshooting and too weak response. Figures 4(c) and 4(d) show that the bandwidth P can be increased well above f_c.

B. *z* feedback

We consider the tip-sample interaction to first order,

$$f_{\text{res}}(z) = f_{\text{res}}^0 + \beta \Delta z,$$

where f_{res}^0 is the resonance frequency at the operating point, Δz is the tip-sample separation, and $\beta = \partial f_{\text{res}} / \partial z$ is an empirical constant known from force-distance measurements.[19] The z feedback uses a PIC with parameters I_z, P_z, and T_z and a characteristic frequency f_z defined in analogy to Eq. (2). We optimize the z-PIC by setting

$$T_z = \frac{1}{2\pi P}, \tag{4}$$

and find that in this case the z-feedback's transfer function $Z(f)$ [cf. Eq. (A7)] is a first-order low-pass filter with bandwidth $\beta P P_z$, which may be much larger than f_c as shown in Figs. 4(e) and 4(f).

We can choose the bandwidth according to surface roughness, scanning speed, and noise requirements by adjusting P and P_z. In our setup the I-U converter is the dominant source of noise which translates into n_φ, the root-mean-square (rms) phase noise measured at the lock-in output. We rms z noise is

$$n_z \approx P P_z n_\varphi. \tag{5}$$

We conclude that if the sensor's characteristic frequency f_c, the phase noise n_φ, and the acceptable z-noise level n_z are given, the feedback parameters P, T, P_z, and T_z are determined by Eqs. (3)–(5). We note that only the product of P
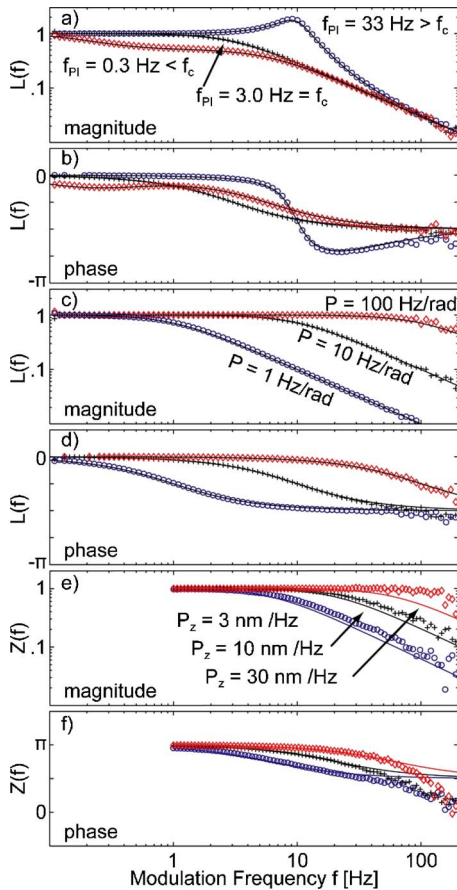
FIG. 4. (Color online) Measurements and theoretical curves (solid lines) for the PLL transfer function $L(f)$ and the z transfer function $Z(f)$ of a sensor with characteristic frequency $f_c = 3$ Hz. (a) and (b): Magnitude and phase of $L(f)$ for $P = 3$ Hz and $T = 500$ ms (red diamonds), $T = 53$ ms (black crosses), and $T = 5$ ms (blue circles). (c) and (d): $L(f)$ for $T = 53$ ms and $P = 100$ Hz/rad (red diamonds), $P = 10$ Hz/rad (black crosses), and $P = 1$ Hz/rad (blue circles). (e) and (f): $Z(f)$ for $P = 45$ Hz/rad, $T = 42$ ms, $\beta = 46$ mHz/nm, $T_z = 3.5$ ms, $P_z = 3$ nm/Hz (blue circles), $P_z = 10$ nm/Hz (black crosses), and $P_z = 30$ nm/Hz (red diamonds).

and P_z enters the equations and that, within reasonable limits, changing their ratio while keeping their product constant will not change the noise on z.

We estimate n_z for a typical set of parameters. The noise of the I-U converter is $n_{IUC} \approx 700$ nV Hz$^{-1/2}$ and a typical output voltage is 250 mV, so that for a lock-in time constant of 150 μs the phase noise is $n_\varphi \approx 10^{-4}$ rad. With $P = 500$ Hz/rad and $P_z = 2$ nm/Hz, we find $n_z \approx 0.1$ nm. This is below the typical surface roughness of 1 nm of our samples and much smaller than our experiments require.

IV. TOPOGRAPHY SCAN

Figure 2(c) shows a topography scan of a nanostructure taken during cooldown 2 (cf. Table I) after 10 weeks of measurements. The sample was prepared by writing oxide lines on the GaAs surface with a SFM at room temperature. The surface was then covered with a thin film of Ti and again oxidized.[20] The topographic resolution is given by the sharpness of the tip, which may deteriorate during long measurements. The resolution of electronic features can be much
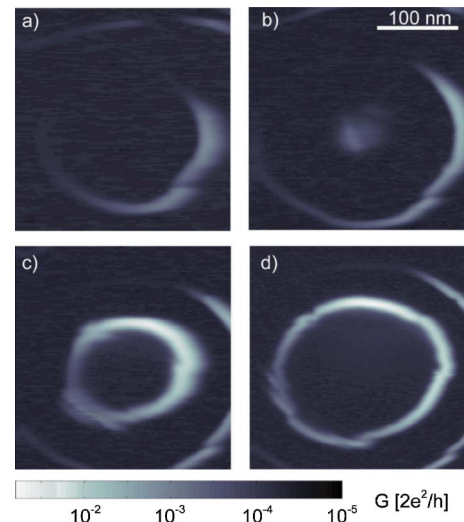

FIG. 5. Conductance of a quantum dot as a function of tip position. The tip voltage is (a) −550 mV; (b) −450 mV; (c) −350 mV; and (d) −250 mV.

better, as seen in Fig. 5. Applying magnetic fields up to 6 T did not change the alignment of sample and sensor.

V. SCANNING GATE MEASUREMENT

Figure 5 shows scanning gate measurements of a quantum dot defined by local anodic oxidation of a GaAs/AlGaAs heterostructure with a 2DEG residing 34 nm below the surface,[20] taken during cooldown 1 (cf. Table I). The dot is in the Coulomb blockade regime, and we scan the tip at a constant height of 100 nm above the surface without oscillating the tuning fork. The quantum dot conductance is mapped as the tip is scanned. While transport is mostly suppressed because of Coulomb blockade, we see characteristic circles of high conductance that grow in diameter as the tip potential is raised.[11–13] The small kinks in the circles are reproducible features due to charge traps in the vicinity of the dot.[21,22]

The tip potential perturbs the energy levels of the dot. If a level comes in resonance with the Fermi levels in the leads, a current can flow and the electron number on the dot changes by 1. The circles are effectively equipotential lines of the tip.

VI. CONCLUSION

We have presented a homebuilt low-temperature scanning probe microscope developed for scanning gate experiments on mesoscopic samples in a dilution refrigerator. We use tuning fork sensors and we have presented a method to optimize the phase-locked loop that detects the sensor's resonance frequency. A topography scan and scanning gate measurements of a quantum dot were shown as examples of successful operation.

The microscope now enables us to perform further experiments on quantum dots in GaAs heterostructures and InAs nanowires with a particular interest in the effects of charge inhomogeneities in the material and the spatial distribution of the wave function inside the dot.

ACKNOWLEDGMENTS

APPENDIX: DERIVATION OF THE FEEDBACK FORMULAS

We begin by discussing the transfer function $k(f)$ of the sensor. It describes how the phase φ measured by the lock-in changes when the driving frequency f_d does not match the sensor's resonance frequency f_{res} which is modulated at a frequency f by a force on the tip,

$$\varphi(f) = k(f)[f_{res}(f) - f_d(f)]. \tag{A1}$$

Following Ref. 23, we write $k(f)$ as a first-order low pass,

$$k(f) = \frac{1}{f_c} \frac{1}{1 + if/f_c},$$

where f_c is defined in Eq. (1) as the sensor's characteristic frequency.

The phase φ is fed into a PIC to calculate the driving frequency $f_d = f_0 + \Delta f_d$, which we write as the sum of a constant f_0 and the small frequency shift Δf_d,

$$f_d(f) - f_0 = \Delta f_d(f) = R(f)\varphi(f). \tag{A2}$$

The transfer function $R(f)$ of a PIC (Ref. 18) is

$$R(f) = P(1 - if_{PI}/f), \tag{A3}$$

with f_{PI} as defined in Eq. (2).

Solving Eqs. (A1) and (A2) for $\Delta f_d(f)$ yields

$$\Delta f_d(f) = \underbrace{\frac{R(f)k(f)}{1 + R(f)k(f)}}_{=:L(f)}[f_{res}(f) - f_0], \tag{A4}$$

where we have defined the PLL's transfer function $L(f)$. Figures 4(a)–4(d) show measurements of $L(f)$ for different combinations of parameters.

$L(f)$ can be measured by modulating f_{res}, which requires applying a small and well-controlled force to the sensor. This is possible but cumbersome. Instead, we modulate f_d because from Eq. (A1) we see that only the difference $f_{res} - f_d$ enters. This can be readily done by software. We demodulate the same signal in the following computation cycle of our digital PLL. This technique requires that $f \ll f_{res}$, which is fulfilled here.

The PLL should be optimized in two ways: It should be as fast as possible without losing stability and it should have a bandwidth that fulfills the requirements of the measurement. Upon inspection of Eq. (A4) we find that for T too large $L(f)$ overshoots, which will lead to an instable and oscillatory feedback, while it will be unnecessarily weak for small T. The optimum is $f_{PI} = f_c$, i.e.,

$$T = \frac{1}{2\pi f_c}.$$

The three cases are shown in Figs. 4(a) and 4(b). In the optimized case $L(f)$ reduces to a first-order low pass with a bandwidth P that can be chosen in the experiment,

$$L(f) = \frac{1}{1 + if/P}.$$

In order to describe the entire feedback loop we start out by writing the resonance shift as a linear function of the tip-surface distance,

$$f_{res} = f_{res}^0 + \beta[\Delta z + \delta z], \tag{A5}$$

where Δz is the piezo position and δz is an external modulation of this distance due to, for example, surface roughness. The z feedback moves the piezo such that the force between tip and surface and hence the frequency shift are constant. We write

$$\Delta z(f) = - R_z(f)[\Delta f_d(f) - \Delta f_d^{set}], \tag{A6}$$

where we have introduced a constant frequency shift setpoint Δf_d^{set} and the transfer function R_z, which describes the z-PIC and has the equivalent form of Eq. (A3) with parameters P_z and T_z. We have included a minus sign to underline that this is a negative feedback.

We can now solve Eqs. (A4)–(A6) to find $Z(f)$, the transfer function of the entire system,

$$\Delta z(f) = - \underbrace{\frac{\beta R_z(f)L(f)}{1 + \beta R_z(f)L(f)}}_{=:Z(f)} \delta z(f). \tag{A7}$$

Using the same arguments as above, we optimize the feedback by setting $f_z = f_{PI}$, i.e.,

$$T_z = \frac{1}{2\pi P}.$$

In this case $Z(f)$ reduces to

$$Z(f) = - \frac{1}{1 + if/(\beta P P_z)},$$

a first-order low pass with a bandwidth of $\beta P P_z$ and a phase shift of π. Figures 4(e) and 4(f) show measurements of $Z(f)$ with optimized parameters for different bandwidths.

We now turn to analyzing noise in the feedback, which in our case is primarily noise on the φ signal coming from the I-U converter. We introduce noise into our description by adding a term to Eq. (A1),

$$\varphi(f) = k(f)[f_{res}(f) - f_d(f)] + n_\varphi(f),$$

where $n_\varphi(f)$ is the noise spectrum of the converter. As before, we can now calculate how this noise transfers to noise on the frequency shift Δf_d and we call this the PLL noise,

$$n_{PLL}(f) = \Delta f_d(f) = \underbrace{\frac{R(f)}{1 + R(f)k(f)}}_{=:\Pi(f)} n_\varphi(f),$$

where $\Pi(f)$ is the noise transfer function. If the noise spec-

trum of the converter is flat and the PLL parameters are optimized in the above sense, then we can integrate $\Pi(f)$ to find that the rms noise is $n_{\text{PLL}} \approx P n_\varphi$. We use Eq. (A7) to calculate how the noise is transferred to noise on the z signal and find that

$$n_z \approx P P_z n_\varphi.$$

Noise and bandwidth are of course also limited by the time constant of the lock-in, which we assumed to be small.

[1] H. J. Mamin, R. Budakian, B. Chui, and D. Rugar, Phys. Rev. Lett. **91**, 207604 (2003).

[2] H. Kambara, T. Matsui, Y. Niimi, and H. Fukuyama, Jpn. J. Appl. Phys., Part 1 **45**, 1909 (2006).

[3] D. Pelekhov, J. B. Becker, and G. Nunes, Appl. Phys. Lett. **72**, 993 (1998).

[4] N. Moussy, H. Courtois, and B. Pannetier, Rev. Sci. Instrum. **72**, 128 (2001).

[5] H. J. Mamin and D. Rugar, Appl. Phys. Lett. **79**, 3358 (2001).

[6] K. R. Brown, L. Sun, and B. E. Kane, Rev. Sci. Instrum. **75**, 2029 (2004).

[7] R. Crook, C. G. Smith, W. R. Tribe, S. O'Shea, M. Y. Simmons, and D. A. Ritchie, Phys. Rev. B **66**, 121301 (2002).

[8] K. Karrai and R. D. Grober, Appl. Phys. Lett. **66**, 1842 (1995).

[9] J. Rychen, T. Ihn, P. Studerus, A. Herrmann, K. Ensslin, H. J. Hug, P. J. A. van Schendel, and H. J. Güntherodt, Rev. Sci. Instrum. **71**, 1695 (2000).

[10] M. A. Topinka, B. J. LeRoy, R. M. Westervelt, S. E. J. Shaw, R. Fleischmann, E. J. Heller, K. D. Maranowski, and A. C. Gossard, Nature **410**, 183 (2001).

[11] M. T. Woodside and P. McEuen, Science **296**, 1098 (2002).

[12] A. Pioda, S. Kicin, T. Ihn, M. Sigrist, A. Fuhrer, K. Ensslin, A. Weichselbaum, S. Ulloa, M. Reinwald, and W. Wegscheider, Phys. Rev. Lett. **93**, 216801 (2004).

[13] P. Fallahi, A. C. Bleszynski, R. M. Westervelt, J. Huang, J. D. Walls, E. J. Heller, M. Hanson, and A. C. Gossard, Nano Lett. **5**, 223 (2005).

[14] B. Hackens *et al.*, Nat. Phys. **2**, 826 (2006).

[15] M. Mendoza and P. A. Schulz, Phys. Rev. B **68**, 205302 (2003).

[16] D. Beck, M. Batzill, C. Baur, J. Kim, and B. E. Koel, Rev. Sci. Instrum. **73**, 1267 (2002).

[17] Nanonis GmbH, www.nanonis.ch

[18] We assume a PIC with a time-domain response, $\Delta f(t) = P\varphi(t) + I\int_{-\infty}^{t} dt' \varphi(t')$.

[19] F. J. Giessibl, Rev. Mod. Phys. **75**, 949 (2003).

[20] M. Sigrist, A. Fuhrer, K. Ensslin, D. C. Driscoll, and A. C. Gossard, Appl. Phys. Lett. **85**, 3558 (2004).

[21] A. Pioda, S. Kicin, D. Brunner, T. Ihn, M. Sigrist, K. Ensslin, M. Reinwald, and W. Wegscheider, Phys. Rev. B **75**, 045433 (2007).

[22] A. E. Gildemeister, T. Ihn, R. Schleser, K. Ensslin, D. C. Driscoll, and A. C. Gossard (unpublished).

[23] T. Ihn, *Electronic Quantum Transport in Mesoscopic Semiconductor Structures* (Springer, New York, 2004).